

Chapter 1

From Magnetodynamics to Spin Dynamics in Magnetic Heterosystems

Claus M. Schneider

Abstract The dynamic behavior of magnetic systems covers a broad range of length and time scales and is of both fundamental interest and technological relevance. The particular challenge in magnetic heterosystems is the need to disentangle the responses of the individual magnetic and chemical components. In this contribution we discuss the results of two complementary experimental approaches addressing element-selective magnetization and spin dynamics. Time-resolved X-ray photoemission electron microscopy (TR-XPEEM) is employed to image the temporal evolution of the magnetization in interlayer exchange-coupled trilayers in the picosecond regime with high lateral resolution. In order to address the femtosecond time scale with element selectivity, we developed a novel pump-probe magneto-optical Kerr effect (MOKE) technique involving higher harmonic generation (HHG) in the extreme ultraviolet regime. We are able to map the spin dynamics of the individual constituents in Permalloy ($\text{Ni}_{80}\text{Fe}_{20}$) with a time resolution of better than 100 fs. Combining PEEM with HHG excitation may pave the way to an element-selective magnetic imaging technique in the lab offering femtosecond time resolution.

1.1 Introduction

The dynamic behavior of magnetic systems involves a wide variety of physical phenomena and covers a broad range of time scales of more than 23 orders of magnitude. Moreover, this enormous dynamic range is also of high technological relevance. The long-term end of the time axis is marked by the data storage retention time defined by the magnetic storage industry. It relates to the thermal stability of a written bit of information for a period of at least 10 years. Another technologically important regime is located between 10^{-9} and 10^{-12} s and governs fast magnetic

C.M. Schneider (✉)

Peter Grünberg Institut (PGI-6), Forschungszentrum Jülich, 52425 Jülich, Germany
e-mail: c.m.schneider@fz-juelich.de

C.M. Schneider

Fakultät f. Physik und CENIDE, Universität Duisburg-Essen, 47048 Duisburg, Germany

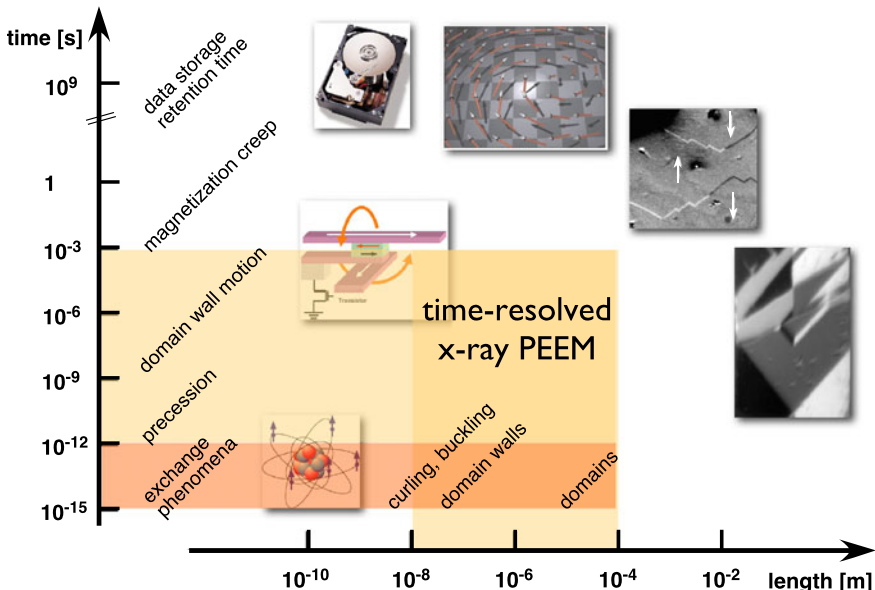


Fig. 1.1 Time and length scales in magnetization and spin dynamics. The *lightly shaded area* marks the region accessible in X-ray photoemission microscopy. The *darker shading* marks a possible extension into the femtosecond region

switching processes (Fig. 1.1). The speed in magnetization reversal and particularly its physical limitations are crucial issues in magnetic data storage and spintronics, as they determine the functionality and frequency response of hard disk drive systems and other devices [1, 2]. The need to increase the data transfer rates in magnetic mass storage devices pushes the relevant switching frequencies far into the gigahertz (GHz) regime. The enormous power dissipation in current semiconductor-based microprocessors spurs the search for low-power alternatives, for example, magnetic logic circuits which provide the advantage of an inherent data non-volatility [3]. The successful operation of future “magnetic processors” at GHz frequencies must be based on a careful control and tuning of the microscopic mechanisms governing the magnetic switching process.

Beyond these technological issues it is particularly the regime of short and ultra-short time scales which combines interesting scientific perspectives with considerable challenges. Pushing the speed of magnetization reversal to its physical limits is only possible if reversal or precessional processes on the nano- and picosecond time scales are understood in detail [4]. However, this understanding will be incomplete without an exploration of the nature of magnetic damping effects [5]. Of specific importance for the details of the dynamic response is also the nature of the excitation, either in the classical manner via a magnetic field pulse, or via spin-transfer torque phenomena involving a spin-polarized current [6].

The femtosecond regime becomes accessible by means of ultrashort-pulse laser sources, which have matured into convenient table-top systems nowadays. The laser

pulses may be employed to strongly excite the electronic system of a sample on a time scale of less than 100 fs [7]. Extending studies of spin and magnetization dynamics into the femtosecond regime has two consequences. First, spin and electron dynamics are intimately connected and can no longer be treated separately. Second, this interplay may open new channels for energy and angular momentum transfer processes. In this limit, the magnetization $\mathbf{M}(\mathbf{r})$ can no longer be represented by a vector of constant length $|\mathbf{M}|$. In order to capture the influence of finite temperature, for example, during ultrafast demagnetization experiments, the vector field $\mathbf{M}(\mathbf{r}, t)$ must include variations of *both* direction and length of the local magnetization vector. Since the pioneering experiments on Ni [8] which revealed an ultrafast demagnetization on the 100 fs time scale driven by strong optical pump pulses, most of the studies have focused on this phenomenon and the underlying microscopic processes. A variety of mechanisms have been invoked, ranging from phonon-, electron-, and magnon-mediated spin-flip processes [9–13], through direct laser-induced spin flips [14] or relativistic spin-light interaction [15] to superdiffusive spin transport [16]. Recently some results appeared which demonstrated a certain control of the magnetization direction by ultrashort light pulses [17–20]. Although the underlying mechanisms still need to be clarified, ultrafast optical switching of magnetic elements may come within reach.

Magnetic heterosystems form the basis for technological magnetic and spintronic devices [21]. Their inherent chemical and magnetic complexity, which also creates coupling phenomena on different length scales, poses another challenge to dynamic studies. In this case we need to disentangle the dynamic responses of the individual magnetic and chemical components in the heterosystems. However, it is generally accepted that even in chemically and magnetically simple confined systems the macrospin picture is often not sufficient to fully describe the dynamic response [22]. This is due to nonuniform magnetization distributions in the transient states or already in the ground state. In order to map the behavior of the magnetization distribution, spatially resolving techniques are needed, and they must be paired with element or chemical selectivity to discriminate the contributions of the individual chemical and magnetic constituents in the heterosystems.

In this contribution we will focus on X-ray photoemission electron microscopy (XPEEM), which has matured into a high-resolution magnetic imaging technique in the picosecond regime. We compile selected results for the dynamic phenomena observed in magnetic heterosystems, and we will discuss a possible extension of the technique into the femtosecond regime.

1.2 Magnetodynamic Imaging on the Picosecond Time Scale

1.2.1 Time-Resolved Photoemission Microscopy

In our experiments we employed time-resolved X-ray photoemission electron microscopy (TR-XPEEM) to image the temporal evolution of the magnetization following a short field pulse excitation. The details of the electron optics of such an

immersion lens microscope have been described in several review articles [23–25]. In general, the instruments fall into two classes differing in the electron-optical concept. The strong electric field between the sample and the objective lens system, which is a characteristic of the immersion lens approach, is realized either by putting the sample on high negative potential or the objective lens on high positive potential. The first solution allows the use of electromagnetic lens elements, but limits the access to the sample. In the second variant, the sample is kept on ground. This is very convenient for magnetodynamics studies, as the sample can be easily subjected to short electrical current and magnetic field pulses generated by fast pulse generators. Thus, this is also the geometry of choice in our experiments.

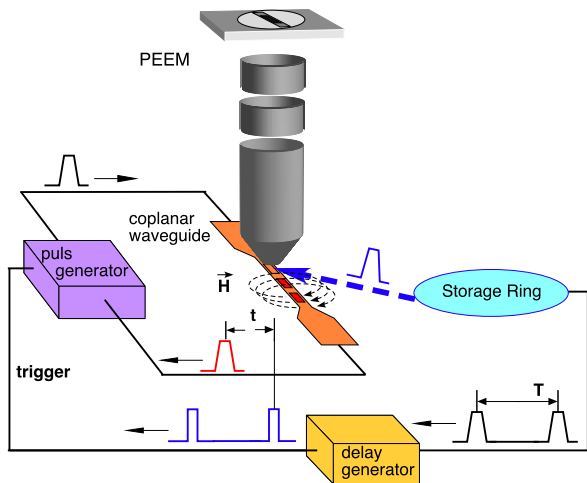
The samples consist of small magnetic elements, which are prepared by optical and electron beam lithography techniques on coplanar waveguides of up to 100 μm width [26]. The high-frequency behavior of the waveguide is chosen so as to provide a close impedance match to commercial pulse generators. The shortest current (*pump*) pulses realized in this way have a rise time of less than 100 ps. For even shorter pulses the waveguide is connected to an Auston switch which can be controlled by a femtosecond pulse laser system. Both the pulse generator and the femtosecond laser are synchronized with the synchrotron radiation pulse train (*probe*) via an electronic circuit which keeps the timing jitter between pump and probe pulses below 10 ps. If the repetition rate of pump and probe pulses is the same, no further selection mechanism in the microscope is needed. In most cases, however, the repetition rate of the pump pulses may be lower in order to allow the magnetic system to return to the ground state after each excitation pulse. In order to select those synchrotron probe pulses which correspond to a given pump pulse sequence, a gating scheme has been implemented in the microscope column [27]. It allows one to blank the electron beam for those synchrotron pulses which do not contribute to the selected time window. The time resolution of this imaging approach being limited by the timing jitter in the electronic synchronization and the pulse width of the synchrotron radiation reaches down to about 10 picoseconds.

The combination of element selectivity and magnetic sensitivity is provided by soft X-ray magnetodichroic phenomena predominantly at the transition metal *L* edges. Magnetic X-ray circular dichroism (MXCD) [28, 29] serves as a contrast mechanism for ferromagnetic samples, whereas magnetic X-ray linear dichroism (MXLD) [30, 31] yields magnetic contrast for certain antiferromagnetic spin structures. The MXCD signal A_C is sensitive to the projection of the magnetization \mathbf{M} onto the helicity vector of the circularly polarized light $\boldsymbol{\zeta}$, i.e.,

$$A_C \sim \mathbf{M} \cdot \boldsymbol{\zeta}. \quad (1.1)$$

Therefore, MXCD yields the highest contrast for \mathbf{M} being oriented parallel or antiparallel to the direction of light incidence. It thus determines a *spin orientation* in space. MXLD, however, depends on the orientation of the spin quantization axis with respect to the electric field vector \mathbf{E} of the linearly polarized light. It therefore can determine only the *spin alignment* direction. The angular dependence in MXLD is usually system dependent and more complicated as crystalline and orbital symmetries have to be considered [32, 33]. The combination of MXCD and MXLD

Fig. 1.2 Principle of a time-resolved PEEM experiment with magnetic field pulse excitation (taken from Ref. [37])



provides convenient access to heteromagnetic systems, as has been demonstrated for static micromagnetic structures in several cases [34–36].

1.2.2 Imaging Magnetization Dynamics in Single Magnetic Thin Films

In order to demonstrate and explain the principle of the time-resolved PEEM technique, we will first focus on results obtained from single magnetic layers.

1.2.2.1 Example I: Permalloy ($\text{Ni}_{80}\text{Fe}_{20}$) Layers

As a first example, we briefly discuss the results obtained on a single Permalloy ($\text{Ni}_{80}\text{Fe}_{20}$) microstructured element of 40 nm thickness, which has been subjected to a 10 ns wide field pulse (Fig. 1.2). The experiments have been performed using the 16-bunch mode at the ESRF, which provides a repetition period of 200 ns [37]. This time structure of the excitation ensures that the magnetization distribution has relaxed into the ground state after each excitation pulse. Each image shown in the sequence of Fig. 1.3 reflects the MXCD contrast at the Ni L_3 edge and represents an average over 10^8 pump-probe cycles. As a consequence, the image shows a clear contrast only in those regions of the magnetization distribution which reproducibly appear at the same lateral position at each pump pulse event. The electrical pulse passing along the coplanar waveguide changes the potential landscape between sample and immersion lens. This leads to a transient change of the imaging magnification; i.e., the image ‘breathes.’ This effect can be conveniently employed to determine not only the reference point on the time axis marking the onset of the

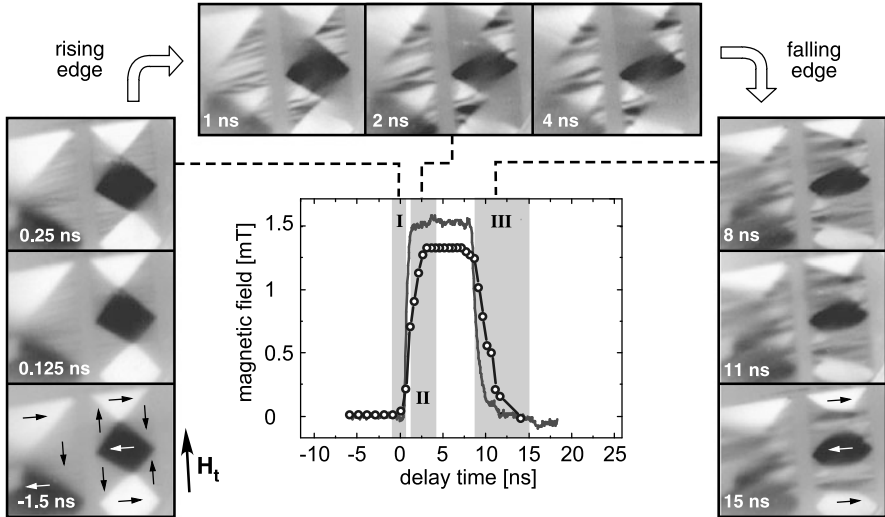


Fig. 1.3 Evolution of the magnetization pattern in a micrometer-sized Permalloy thin film element following the excitation with a magnetic field pulse. The pulse shape supplied by the pulse generator (*solid line*) is only slightly broadened, when the pulse (\circ) arrives at the element. The *arrows* indicate the orientation of the local magnetization vector. From [37]

magnetic field pulse, but also the pulse shape of the magnetic excitation (data points in Fig. 1.3) [38].

The image shows the domain distribution in a rectangular element (right, $16 \times 8 \mu\text{m}^2$) and part of a square element (left, $16 \times 16 \mu\text{m}^2$). In the ground state, i.e., before the field pulse sets in, the elements assume simple Landau flux closure domain structures. This indicates that the domain pattern is dominated by the tendency of the system to reduce the magnetic stray field outside the particle. The arrows indicate the orientations of the local magnetization vector in the individual domains. As soon as the magnetic pulse field $\mathbf{H}_p(t)$ acts on the element, the domain configuration starts to change in a characteristic manner (region I). In the following, we will denote the ground state magnetization distribution at delay time $t < 0$ by $\mathbf{M}_0(\mathbf{r})$ and the transient magnetization distribution at $t > 0$ by $\mathbf{M}_t(\mathbf{r})$. The most pronounced changes appear in those triangular domains for which the ground state magnetization direction points antiparallel to the pulse field, $\mathbf{M}_0(\mathbf{r}) \downarrow \uparrow \mathbf{H}_p(t)$. Exhibiting an intermediate gray contrast level in the ground state, they develop a clear stripe-like pattern, which indicates the formation of a network of small domains with transient magnetization $\mathbf{M}_t(\mathbf{r}) \perp \mathbf{H}_p(t)$. This phenomenon is known as incoherent magnetization rotation [39].

A coherent magnetization rotation, by contrast, appears in those domains whose ground state magnetization fulfills $\mathbf{M}_0(\mathbf{r}) \perp \mathbf{H}_p(t)$, because they are subject to the highest magnetization torque $\tau(\mathbf{r}, t) \sim \mathbf{M}(\mathbf{r}) \perp \mathbf{H}_p(t)$. They appear as black and white contrast levels in the images. In particular in the regions of the 90° -domain walls separating domains with $\mathbf{M}_0(\mathbf{r}) \perp \mathbf{H}_p(t)$ and $\mathbf{M}_0(\mathbf{r}) \parallel \mathbf{H}_p(t)$, the magnetiza-

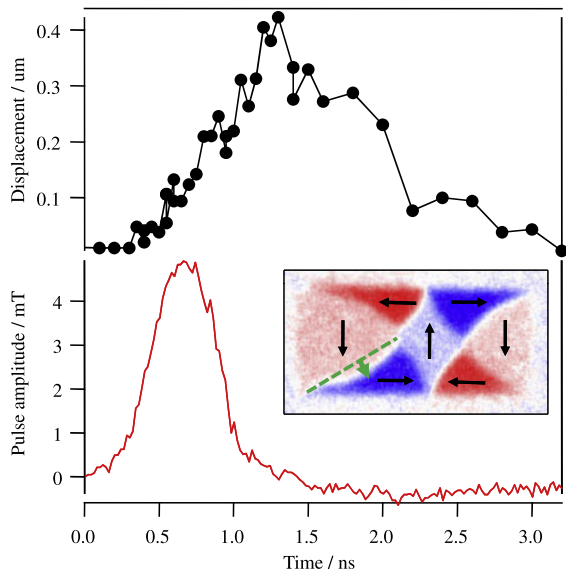
tion rotates, effectively increasing the area of the domains with $\mathbf{M}_0(\mathbf{r}) \parallel \mathbf{H}_p(t)$. As a consequence the domain wall seems to smear out. This process is most pronounced close to the central vortices and weaker at those positions where the domain wall meets the boundary of the element. The edges of the element act as pinning sites for the domain walls and stabilize the local magnetization against the coherent rotation. Consequently, on the plateau of the field pulse (region II), the domain with $\mathbf{M}_0(\mathbf{r}) \parallel \mathbf{H}_p(t)$ has taken a W-like shape, whereas the black and white domains with $\mathbf{M}_0(\mathbf{r}) \perp \mathbf{H}_p(t)$ have reduced in size. We also note that most of these changes take place along the rising edge of the field pulse during the first few hundred picoseconds.

On the plateau of the field pulse the transient domain structure stabilizes, as can be seen by comparing the MXCD images taken at delay times $t = 2$ ns and $t = 4$ ns. A temporary equilibrium state is formed, which is determined by the local effective field $\mathbf{H}_{\text{eff}}(t) = \mathbf{H}_{\text{dip}}(t) + \mathbf{H}_p(t)$, which contains the contributions of the dipolar and pulse fields. This configuration has an important consequence which becomes visible along the falling edge of the field pulse. The reduction of the pulse field also causes a formation of the stripe-like phase in the previously unaffected regions with $\mathbf{M}_0(\mathbf{r}) \parallel \mathbf{H}_p(t)$. This behavior can be understood in the following manner: The reduction of the pulse field acts on the temporary equilibrium state as if a hypothetical magnetic field $\mathbf{H}_{\text{hyp}}(t)$ is applied into the direction opposite to $\mathbf{H}_p(t)$. The W-shaped domains with $\mathbf{M}_0(\mathbf{r}) \parallel \mathbf{H}_p(t)$ are then subject to the condition $\mathbf{M}_t(\mathbf{r}) \downarrow \uparrow \mathbf{H}_{\text{hyp}}(t)$, which also causes an incoherent magnetization rotation in these domains. As a consequence, the stripe-like areas expand through the entire element. As this process involves the creation of many partial domain walls, the resulting structure is relatively stable, even after the field pulse has completely decayed. The domain wall motion is considerably slower than the magnetization rotation. Therefore, it takes more than 10 ns for the transient magnetization configuration to relax back into the ground state.

1.2.2.2 Example II: Fe(001) Layers

In contrast to the polycrystalline Permalloy thin films described above, single crystal layers usually possess a strong magnetocrystalline anisotropy. This has important consequences, as demonstrated in Fig. 1.4. The sample comprises a $20 \times 10 \mu\text{m}^2$ sized Fe(001) thin film element (thickness 10 nm), which has been grown on a Ag(001) coplanar waveguide on a GaAs(001) substrate. It is well known that the magnetocrystalline anisotropy requires the easy axes of magnetization in single-crystalline iron to lie along the [001] crystalline directions [41]. The element has been structured such that the easy axes agree with the boundaries of the elements. Therefore, the ground state domain pattern is very similar to the pattern of the Permalloy element discussed before, because magnetocrystalline and dipolar (shape) anisotropy act in the same directions. The direction of light incidence is pointing along the long axis of the element, generating the strongest magnetodichroic contrast from the top and bottom triangular domains. The domain pattern

Fig. 1.4 Domain wall bulging in a $20 \times 10 \mu\text{m}^2$ Fe element (inset) as a response to the magnetic field pulse (bottom). Arrows indicate local magnetization direction. Broken green line marks the position of the domain wall in the ground state, i.e., the static case. From [40]



is reproduced in a false color representation (blue–red instead of black–white) to highlight small changes occurring during the dynamic response.

The field pulse in the dynamic experiment (pulse field $\mathbf{H}_p(t)$) is pointing from top to bottom along the short axis of the element) is shorter by a factor of 10 than that in Fig. 1.3. Thus, we first verified that incoherent rotation also occurs in Permalloy films under these conditions [40]. The most obvious finding in Fe(001) is thus the *absence* of incoherent rotation processes. Evidently, the field pulse is not strong enough to overcome the magnetocrystalline anisotropy and to locally rotate the magnetization out of the easy axis. The field pulse generates the largest magnetization torque in the blue and red colored domains. This leads to a coherent magnetization rotation in these domains, which in turn leads to a *bulging* of the domain walls with respect to the ground state configuration.

In Fig. 1.4 we have analyzed this behavior more quantitatively by plotting the time dependence of the displacement in the center of the wall normal to the wall axis. The comparison to the shape of the field pulse reveals an astonishing finding: There is a considerable time lag between the field pulse and the wall response. In particular, the maximum of the bulging motion is located at around $t \approx 1.2$ ns, i.e., a delay time at which the field pulse itself has already decayed. More quantitatively, there is a time delay of $\tau_B = 700$ ps between the maximum of the field excitation and the maximum domain wall displacement. This behavior can be attributed to the interplay of two mechanisms. First, the field pulse stores Zeeman energy in the magnetization distribution which in the low-anisotropy material Permalloy leads to large-angle rotations of the local magnetization. The stronger magnetocrystalline anisotropy in Fe(100) suppresses large-angle rotations and leaves only the much slower domain wall motion as a pathway to reduce the energy of the system. Thus, the wall bulging proceeds as long as it is driven by the excess energy in the spin sys-

tem. Second, the long decay of the excitation is also promoted by a small magnetic damping in iron for which a Gilbert damping factor of $\alpha = 3 \times 10^{-3}$ has been reported [42]. The characteristic time scale on which the Zeeman energy is dissipated via domain wall motion is given by [43]

$$\tau_{\text{DW}} = \frac{1}{\gamma \mu_0 M_S \alpha} \quad (1.2)$$

with γ denoting the gyromagnetic ratio. Taking the value $\mu_0 M_S = 2.2$ T for the saturation magnetization of iron yields a time constant of $\tau_{\text{Fe}} = 850$ ps, which compares favorably with the preceding value of $\tau_B = 700$ ps. A further analysis of the time dependence in Fig. 1.4 reveals that the domain wall bulging builds up with an almost constant wall velocity of $v_w \approx 400$ m/s, but relaxes significantly more slowly with a domain wall speed of $v_w \approx 100$ m/s. The constant wall velocity in the initial rise may be due to the Walker limit [44]. The Walker breakdown field in iron is estimated to be about 3.3 mT, which agrees well with the external field value at the position where the domain wall velocity levels off into a constant value. We have also verified the main results of our interpretation by means of micromagnetic simulations within the OOMMF environment [45].

1.2.3 Imaging Magnetization Dynamics in Interlayer-Coupled Trilayers

After seeing the variety of dynamic processes which can be revealed by photoemission microscopy on single magnetic layers, we can take the technique a step further to investigate more complicated magnetic heterostructures. In the following we are focusing on trilayer structures composed of two different ferromagnetic layers FM1 and FM2 sandwiching a nonmagnetic interlayer. Exploiting the well-known phenomena of interlayer exchange coupling [46, 47], we can tune the magnetic coupling character between FM1 and FM2 from ferromagnetic to antiferromagnetic by adjusting the thickness of the interlayer appropriately. In this way we can study the influence of the interlayer coupling onto the magnetodynamics, but we must be able to separate the response of the two layers FM1 and FM2. This is achieved via the element selectivity of the MXCD effect if both layers have different chemical constituents and the thicknesses of the top layer and interlayer are in the nanometer regime. In this case the magnetodichroic signal resulting from the bottom layer can still be discerned.

Our magnetodynamics studies encompassed several material systems comprising layers of single magnetic elements or binary compounds [48–50]. In the following we will discuss results on the dynamic response obtained from a polycrystalline trilayer of the type Fe₂₀Ni₈₀(2nm)/Cr(2.5nm)/Fe₅₀Co₅₀(5nm). In this case, the interlayer coupling is weak and leads to a ferromagnetic alignment of the local magnetization direction of both layers. This can be seen in Fig. 1.5, which displays MXCD maps taken at the Ni and Co L₃ absorption edges, which directly translate into the

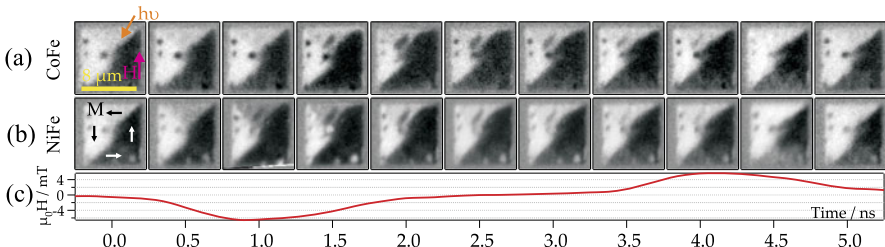


Fig. 1.5 Evolution of the layer-resolved magnetization patterns in a micrometer-sized pseudo-spin valve element following the excitation with a bipolar magnetic field pulse. The layer structure comprises $\text{Fe}_{20}\text{Ni}_{80}$ (2 nm)/Cr(2.5 nm)/ $\text{Fe}_{50}\text{Co}_{50}$ (5 nm). From [50]

magnetization distribution of the top and bottom magnetic layers, respectively. A direct comparison of the domain patterns at delay time $t = 0$ reveals the same contrast distribution and hence a ferromagnetic coupling between the $\text{Fe}_{20}\text{Ni}_{80}$ and the $\text{Fe}_{50}\text{Co}_{50}$ layers. The domain pattern corresponds closely to a Landau–Lifshitz flux closure pattern with four triangular domains and a central vortex (cf. Fig. 1.3). The magnetization vectors in all four domains make an angle of about 45° and therefore have about the same projection onto the direction of light incidence. Because of the angular dependence of the MXCD, the left and top and the right and bottom domains, respectively, show almost the same magnetic contrast. The dark circular dots appearing in the left-hand domain are defects on the sample surface.

This pseudo-spin valve structure is subjected to a magnetic field pulse with a maximum amplitude of 6 mT. We found out that a unipolar pulse often left the system in a metastable transient state which severely impairs a repetitive pump-probe measurement. Apparently, the restoring force by the demagnetizing field was not strong enough to restore the initial state before the pulse excitation, in contrast to the observation in single Permalloy layers. Only a bipolar pulse ensured that the system reproducibly returned back to the initial state even after a train of 10^9 repetitive field pulses. and bottom the element-resolved magnetization character determines the dynamic response.

Following the temporal evolution of the magnetization pattern in the Permalloy and $\text{Fe}_{50}\text{Co}_{50}$ layers, we can discern three different processes taking place on different time scales. The fastest response takes place in the top and bottom domains and appears as a change of the contrast level in the entire domain. This contrast change is related to a rotation of the local magnetization vector in the direction of the external or rather effective magnetic field (see also Fig. 1.6(a)). The second process, which takes place on a longer time scale, is a domain wall propagation which causes the domain with $\mathbf{M}_0(\mathbf{r}) \parallel \mathbf{H}_p(t)$ to expand at the expense of the neighboring domains (cf. Fig. 1.6(b)). The third process is slowest and leads to the nucleation and expansion of a small domain in the top domain (cf. Fig. 1.6(c)). Judging from the contrast level, the magnetization vector in this domain is also parallel to the external field.

Although at first glance the responses look similar for the top and bottom ferromagnetic layers, a closer inspection of the data in Fig. 1.3 reveals an interesting difference, which gives more insight on the microscopic mechanisms governing the

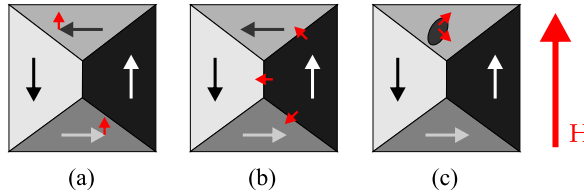


Fig. 1.6 Graphical representation of the magnetodynamic response taking place in different parts of the domain patterns displayed in Fig. 1.5: (a) magnetization rotation, (b) domain wall displacement, and (c) domain nucleation and growth. The respective direction of motion is indicated by the small red arrows in panels (a) to (c)

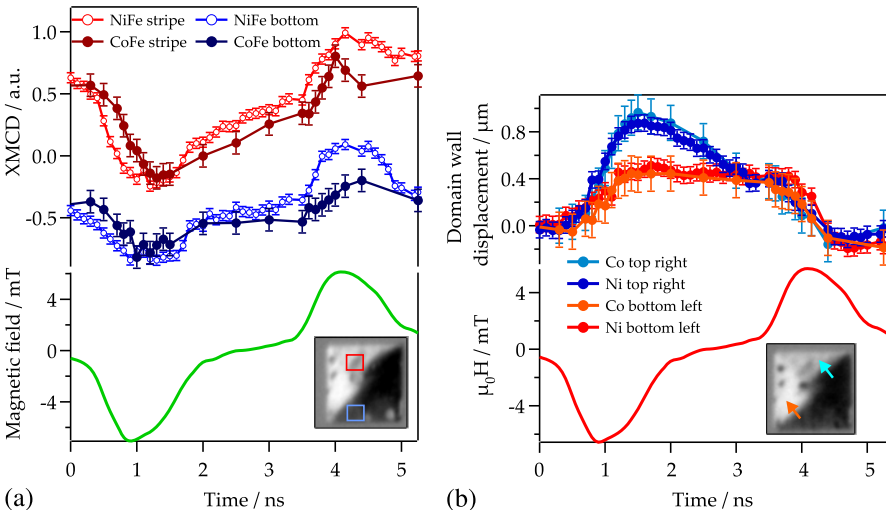


Fig. 1.7 (a) Evolution of the magnetization rotation in the top and bottom domains along the magnetic field pulse for the top (Permalloy) and bottom ($\text{Fe}_{50}\text{Co}_{50}$) layers (squares mark the area of averaging). (b) Layer-resolved domain wall motion (position indicated by the arrows) driven by the magnetic field pulse. From [48]

magnetization dynamics. In the following we will focus on the magnetization rotation and the domain wall motion. Figure 1.7 compiles a quantitative assessment of the two processes, which is based on the analysis of the temporal variation of the MXCD contrast levels in both ferromagnetic layers.

The temporal evolution of the magnetization rotation in both magnetic layers is compared in Fig. 1.7(a). The data have been obtained by averaging the magnetic contrast over an extended area in the top and bottom triangular domains. The rotation angle of \mathbf{M} was then determined from the angular dependence of the MXCD signal (cf. (1.1)). At the onset of the field pulse (negative excursion) the rotational motion also sets in and increases with the magnetic field. However, there is a characteristic phase shift between the responses in the two layers. The rotation in the FeCo layer lags behind that in the Permalloy layer by about 250 ps. This time lag also

affects the further temporal development, as the relaxation in the CoFe layer is also delayed and the rotation in the CoFe layer is smaller during the positive excursion of the field pulse. This behavior is similar for both the top and the bottom domains. As a consequence, the magnetization vectors \mathbf{M}_{FeNi} and \mathbf{M}_{CoFe} are not rotating as a unit, but develop a dynamic twist during the magnetic field pulse excitation. The interpretation of this behavior can be traced back to the coercive fields of the individual layers, which differ by about a factor of 10 ($H_{\text{C,FeNi}} = 0.5 \text{ mT}$, $H_{\text{C,CoFe}} = 5 \text{ mT}$). According to the empirical model of Doyle et al. [51], the switching time τ can be related to the layer-specific coercivity $H_{\text{C},n}$,

$$\frac{1}{\tau} = \frac{1}{S_w}(H - H_{\text{C},n}), \quad (1.3)$$

of the respective layer n via the switching coefficient $S_w \approx 2(1 + \alpha^2)/(\alpha\gamma)$. The above quasi-statically determined coercivity values can be regarded as lower bounds only to the dynamic coercivity [52], which precludes any quantitative interpretation. Qualitatively, however, the switching time in the CoFe layer should be significantly higher than in the Permalloy layer, in agreement with the experimental observation.

The data on the domain wall motion along the field pulse are compiled in Fig. 1.7(b) and exhibit a different behavior. A comparison of the motion in the FeNi and CoFe layers reveals a different amplitude, but the same time dependence during the negative part of the bipolar field pulse. In particular, there is no time delay in the initial phase of the domain wall motion; i.e., the domain walls in the top and bottom layers move simultaneously. This may be understood by the fact that a domain wall generates an additional stray field, which can increase the effective coupling through the nonmagnetic interlayer [53]. Also, keep in mind that the domain wall motion is considerably slower than the magnetization rotation. The scatter in the experimental data points may simply mask a potential difference of the order of 100 ps in the onset of the domain wall displacement in Fig. 1.7(b). The finite domain wall velocity also causes the system to relax slowly and still be in a transient state when the positive component of the magnetic field pulse starts to act. Consequently, we observe only a weak domain wall displacement in the opposite direction, although the positive and negative components of the bipolar pulse are of comparable magnetic field strength.

1.3 Addressing the Femtosecond Time Scale

The area of magnetization dynamics discussed in the previous section reaches its limits in the picosecond regime. The fastest process available in this regime is the precessional motion of the magnetization vector, which is well described by the Landau–Lifshitz–Gilbert (LLG) equation. An important precondition in the LLG treatment is that the length of the magnetization vector remains essentially unchanged during the motion, i.e., $|\mathbf{M}| = \text{const.}$

Pioneering laser experiments in the mid-1990s showed that there may be even faster excitation channels resulting in magnetization or rather spin dynamics down

to the femtosecond regime [8]. In this case the magnetic system is excited by a strong light pulse from an amplified femtosecond pulse laser, e.g., a Ti:sapphire oscillator. This light pulse may be as short as 50 fs and transfers an energy of up to several microjoules (μJ) to the magnet. The wavelength of this pump pulse is usually around $\lambda = 800 \text{ nm}$; i.e., it leads to excitations of electrons mainly around the Fermi level resulting in a transient nonequilibrium electron distribution which differs strongly from the Fermi distribution in thermodynamical equilibrium. This situation also affects the magnetic order, i.e., the spin system. Consequently, an ultrafast demagnetization, i.e., a reduction of the magnetization vector on a time scale of the order of 100 fs, takes place. In other words, in these experiments the magnetization vector is no longer of constant length, but rather varies in time, i.e., $|\mathbf{M}| = f(t)$. The interpretation of such experiments usually follows the three-temperature model [8, 54], in which the solid is described by three interacting subsystems with well-defined temperatures for the electron (T_e), spin (T_s), and lattice (T_l) subsystems. This phenomenologically derived model assumes an ultrafast dissipation channel for the spin angular momentum in order to explain a demagnetization time of a few hundred femtoseconds. Various approaches are currently discussed controversially to explain such a fast spin-flip process; among them are inelastic magnon scattering, Elliot–Yafet type mechanisms [11], photon-induced spin flips [14, 55], spin-flip Coulomb scattering [10], and relativistic quantum-electrodynamic processes [15]. On the other hand, spin-dependent transport processes driven by the nonequilibrium electron distribution may generate sizable contributions to the ultrafast demagnetization without invoking an angular momentum dissipation channel at all [16, 56]. Moreover, recent theories suggest that the demagnetization time τ_M is related to the Gilbert damping factor α [57], which also appears in the LLG equation.

Recently, an ultrafast all-optical switching of the magnetization has been reported in GdFeCo alloys. In this case the magnetization is found to reverse its orientation by 180° as a response to the irradiation with a circularly polarized femtosecond laser pulse [19]. Whether this effect involves the ultrafast demagnetization or is related to other microscopic mechanisms is currently still a matter of intense debate. In any case, the preceding examples show that spin dynamics on ultrafast time scales is a highly interesting area of research. All of the ultrafast experiments performed up to now, however, lack lateral resolution. Investigating ultrafast spin dynamics with photoemission microscopy is a real challenge and requires several experimental problems to be solved. Two of them—the questions of an appropriate light source for femtosecond pulses and a suitable magnetic contrast mechanism—will be addressed below.

1.3.1 Femtosecond Pulse Soft X-Ray Sources

In order to introduce element selectivity into ultrafast spin dynamics studies, we need soft X-ray light sources providing femtosecond pulses. At present, this quality of radiation can be provided by at least three different types of sources: (i) free electron lasers (FELs), (ii) femtosecond slicing procedures, and (iii) higher harmonic

generation (HHG). Free electron lasers provide femtosecond light pulses with an extremely high peak brilliance which is a factor of up to 10^7 higher than that of storage ring light sources [58]. This corresponds to up to 10^{13} photons per 30 fs pulse. On the one hand, this photon density may lead to severe sample damage even after a single-shot exposure [59]. On the other hand, in electron-based spectroscopies and microscopies the peak brilliance translates into a high photoelectron density which may lead to space-charge phenomena resulting in severely deteriorated spectral and lateral resolution of the instruments [60]. At the other end of the photon density scale we find the femtosecond slicing approaches [61]. They are based on the modulation of the electron bunches in the storage ring by means of intense photon pulses from an external laser source. The limited efficiency of this slicing technique results in very low photon fluxes, but allows for repetitive pump-probe experiments. The first results on element-selective studies of ultrafast demagnetization at the L_3 edges of Ni have been obtained recently [62, 63]. Nevertheless, the complexity of the slicing experiment and the rather limited accessibility to such a source at the moment allow only for selected experiments.

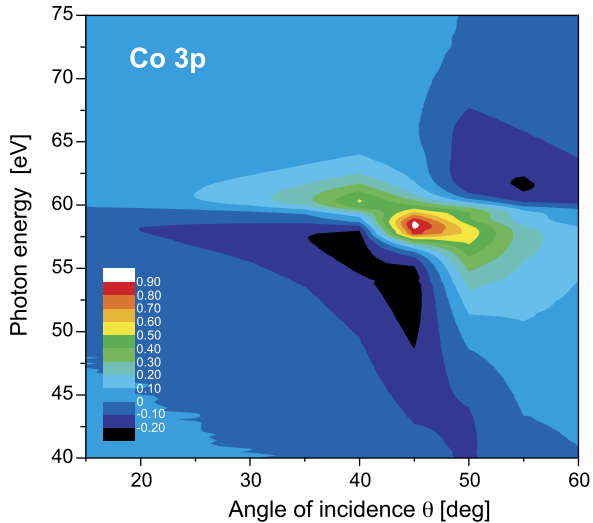
In contrast to the accelerator-based sources described above, the HHG technique involves essentially a table-top laser setup. The pulses of a Ti:sapphire amplifier are focused into a noble gas medium such as Ar or Ne. The strong electromagnetic field of the light pulse causes the valence electrons to oscillate in the Coulomb potential of the core with partial ionization and recombination events. During the recombination photons of higher energies corresponding to integer multiples of the fundamental laser energy are emitted [64]. With argon as a medium the higher harmonic upconversion may easily reach photon energies of 100 eV (the phase-matching cut-off for Ne), thereby covering the transition metal M absorption edges. This energy range is also often referred to as extreme ultraviolet (EUV). The radiation produced by the HHG process retains the polarization and coherence properties of the driving laser and may reach pulse lengths down to less than 10 fs [65]. In addition, each HHG light pulse has a well-defined phase relation to the corresponding light pulse at the fundamental wavelength, therefore providing the means for inherently synchronized pump-probe experiments with femtosecond time resolution.

1.3.2 Magnetodichroic Effects in the EUV Regime

In order to perform element-selective studies in the EUV regime, an appropriate magnetodichroic phenomenon is needed which delivers a magnetic signal at these photon energies. As the HHG source provides only linearly polarized light, MXCD-type effects like those used in the PEEM experiments described above are not accessible. However, studies on iron with synchrotron radiation by Pretorius et al. have shown that an effect similar to the transverse magneto-optical Kerr effect (T-MOKE) can be observed in resonant excitation at the Fe M edge [66].

In Fig. 1.8 we show corresponding data for such a resonant reflectivity experiment on a thin Co film using linearly polarized synchrotron light. The electric

Fig. 1.8 Magnetic resonant reflectivity in the EUV regime at the Co M edge as a function of scattering angle and photon energy. The color encodes the value of the magnetodichroic asymmetry A_R



field vector of the linearly polarized light is oriented within the scattering plane, whereas the magnetization vector is oriented perpendicular to this plane. The magnetodichroic signal in reflection is displayed as an asymmetry

$$A_R = (I^+ - I^-)/(I^+ + I^-) \quad (1.4)$$

with I^+ and I^- denoting the intensity of the reflected light for opposite directions of the magnetization or external magnetic field. The variation of A_R with angle of incidence θ and photon energy $\hbar\omega$ reveals a pronounced maximum at around $\hbar\omega \approx 58$ eV, close to the position of the Co 3p core level, and $\theta \approx 45^\circ$, corresponding to the Brewster angle. Under these conditions the magnetodichroic signal A_R reaches peak values of more than 90 %. This property makes the resonant magnetic reflectivity or T-MOKE in the EUV regime a very useful tool for the study of magnetic heterosystems [67, 68].

This is briefly demonstrated in Fig. 1.9, which shows the spectral distribution of the HHG light reflected off a Permalloy grating and the corresponding T-MOKE asymmetry A_R . The HHG intensity spectrum exhibits the characteristic comb structure and covers both the Fe and Ni M edges. A reversal of the magnetization direction introduces a strong change in the harmonics, particularly around $\hbar\omega \approx 66$ eV, corresponding to the Ni edge. Similar changes occur at the Fe edge at around $\hbar\omega \approx 54$ eV. This is also reflected in the magnetodichroic asymmetry, which exhibits pronounced maxima at these two photon energies. The sign of the asymmetry is the same for both edges and underlines the fact that the Fe and Ni magnetic moments are strongly exchange-coupled in the alloy and align parallel to each other. We also compare the HHG data to measurements with synchrotron radiation performed on the same sample system and note an overall fair agreement. The remaining differences in the asymmetry spectra are due to differences in the experimental geometry in the HHG and synchrotron experiments.

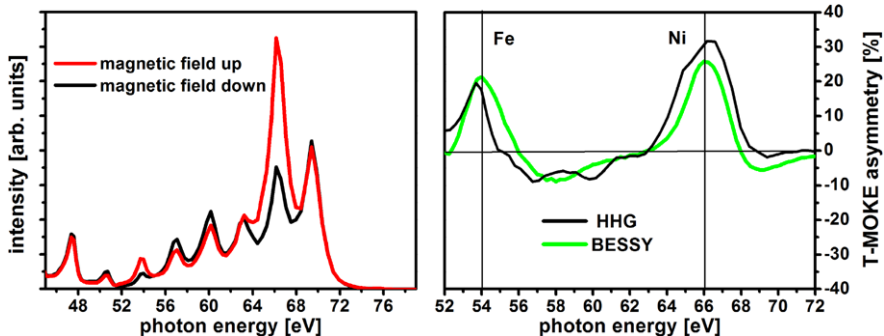


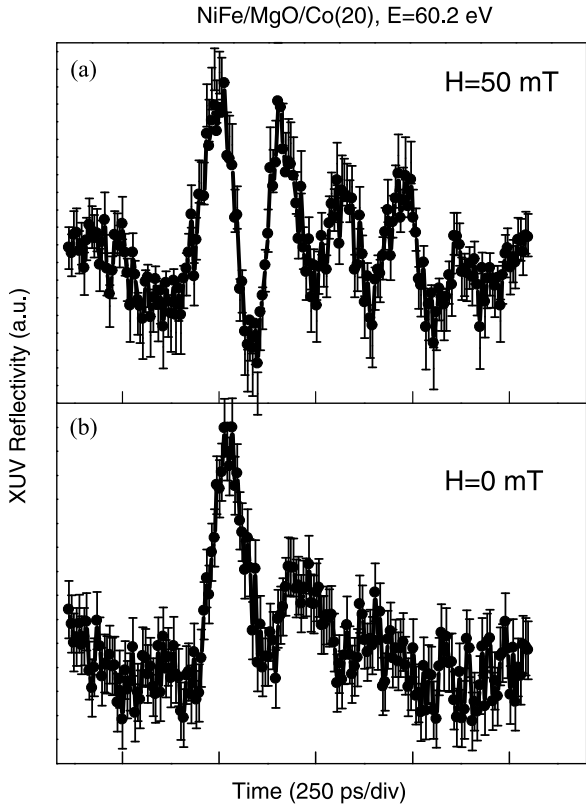
Fig. 1.9 Magnetic resonant reflectivity in the EUV regime at the Fe and Ni M edges in a Permalloy layer. Intensity distribution for opposite magnetization directions (*left*) and resulting magnetodichroic asymmetry (*right*) acquired with HHG and synchrotron radiation

In performing synchrotron pump-probe reflectometry experiments we have also already answered the question of to what extent this EUV T-MOKE signal can also be used for magnetodynamics studies in the picosecond regime [69]. For this purpose, we prepared magnetic heterosystems on a coplanar waveguide with an integrated Auston switch on GaAs substrates. The switch was driven by a Ti:sapphire fs-pulse laser (pulse width 20 fs) electronically synchronized with the synchrotron radiation pulses (50 ps FWHM) and generated magnetic field pulses of 10 ps (FWHM) at a repetition frequency of 100 MHz. These short field pulses caused a small-angle precession of the magnetization in the Permalloy and Co layers, which was recorded by the time traces in the element-selective T-MOKE signals, which are reproduced for the Co layer in Fig. 1.10. These time traces reflect the contribution of several precessional modes, the ratio of which can be changed by a static external field, as clearly visible in the experimental data. Although in the case of the small-angle precession the change in the resonant magnetic reflectivity signal is much smaller than for a full magnetization reversal (cf. Figs. 1.8 and 1.9), it can be conveniently used to map the temporal evolution of the precessional motion and distinguish different excitation modes.

1.3.3 HHG Pump-Probe Experiments

An experiment addressing ultrafast demagnetization in an element-selective manner without lateral resolution is sketched in Fig. 1.11. Both the HHG radiation and the fundamental pump pulse are focused by a toroidal mirror onto the sample. The sample comprises a Permalloy ($\text{Ni}_{80}\text{Fe}_{20}$) film which has been microstructured into an optical grating. It is placed into a Helmholtz coil system which generates the magnetic field for magnetization reversal. The sample disperses the HHG spectrum onto a CCD camera; the fundamental light at a wavelength of $\lambda = 760$ nm is blocked by

Fig. 1.10 Time-resolved T-MOKE signal of the Co(20)/MgO/NiFe sample at the Co M absorption edge (60.2 eV) and for static external magnetic fields 50 mT (a) and 0 mT (b). From [69]



an Al filter. In this way the magnetic dichroism can be measured in parallel for all relevant photon energies.

The results on the ultrafast demagnetization from this Permalloy sample are shown in Fig. 1.12. The data represent the time evolution of the magnetodichroic response at the Fe and Ni edges, and at a point in between the edges where the magnetodichroic signal disappears (the positions of the respective harmonics are indicated in the inset). In the temporal evolution we observe the fast reduction of the magnetodichroic response on a time scale of about $\tau_M \approx 150$ fs, followed by a much slower recovery of the signal due to spin-lattice relaxation. At the photon energy $\hbar\omega \approx 58$ eV there is no change of the dichroic signal. Within the experimental uncertainty, the demagnetization times for Fe and Ni appear the same. At first glance, this seems plausible because of the strong exchange coupling in this intermetallic compound which ties the magnetic moments of Fe and Ni together. However, recent studies with improved time resolution suggest that a small difference in the demagnetization of different constituents in a heteromagnetic system may exist. In the Permalloy system a small time delay of the order of a few tens of femtoseconds is observed for the onset of demagnetization of Ni and Fe [71]. This results in the Ni demagnetization lagging behind the Fe demagnetization in a char-

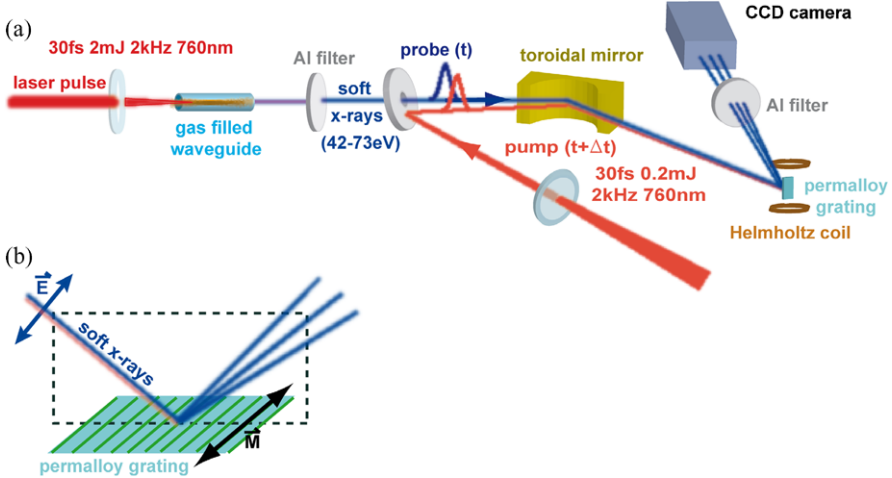
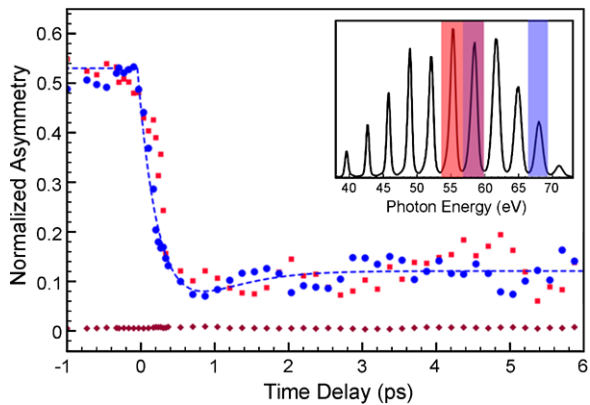


Fig. 1.11 Setup of the HHG pump-probe experiment **(a)**. The sample itself serves as an optical grating to disperse the radiation onto a CCD camera **(b)**. From [70]

Fig. 1.12 Ultrafast demagnetization in Permalloy ($\text{Ni}_{80}\text{Fe}_{20}$) measured element-selectively at the Fe (red) and Ni (blue) M absorption edges. The purple data points refer to a photon energy of $\hbar\omega \approx 58$ eV, where the magnetodichroic signal disappears. Inset: HHG spectrum with color markers for the harmonics selected for the element-selective data acquisition. Taken from [72]



acteristic fashion. Reducing the exchange coupling between Fe and Ni by doping with Cu increases this time lag, the microscopic origin of which still needs to be explained.

In the context of magneto-optical pump-probe techniques often the question arises as to what extent the magneto-optical signal—in our case the T-MOKE asymmetry—represents changes in the magnetization rather than changes in the electronic structure. This is a nontrivial issue, as the pump pulse puts the electron system in a nonequilibrium state which may affect the optical response and the magneto-optical coupling constants. It turns out that it is possible to avoid most of those optical side effects by taking advantage of the fact that they are symmetric under magnetic field reversal, whereas the magnetic contribution is antisymmetric. Therefore, in magneto-optical pump-probe experiments, the magnetic response

of the sample is extracted by taking the sample response for two magnetic fields aligned in opposite directions; subsequently, assuming that the optical constants are not affected by the magnetic field, the optical response can be eliminated by subtracting the two responses. A thorough discussion of possible effects influencing the magneto-optical response can be found in [73]. The question of whether the signal from the T-MOKE at the $M_{2,3}$ edges of a magnetic material is purely magnetic or is perturbed by nonmagnetic artifacts was addressed in detail in [74]. There it was shown that the magnetic asymmetry obtained with EUV photons in the T-MOKE geometry is predominantly of magnetic origin and that any transient nonmagnetic contribution to the asymmetry parameter is small (0.2 %) compared to the amplitude of the demagnetization changes (20 %) at the same pump fluence. This highlights the importance of T-MOKE in the EUV regime for the investigation of ultrafast magnetization dynamics.

1.3.4 Future Development

The T-MOKE phenomenon described in Sect. 1.3.2 has a pronounced angular dependence as is apparent from Fig. 1.8, with the maximum asymmetry appearing around a 45° angle of light incidence. In PEEM experiments the angle of light incidence ranges between 15° and 25° depending on the instrument's geometry. At these angles the T-MOKE signal in the reflected light is significantly reduced, which opens up a possibility for magnetodichroic effects in the absorption channel. In a pioneering PEEM experiment Hillebrecht et al. have shown indeed that even under these geometrical constraints a sizable magnetodichroic signal of up to 5 % in the total electron yield appears and can be successfully employed for magnetic domain imaging [75]. On the other hand, PEEM imaging even with light pulses as short as 200 as has been demonstrated recently [76]. In this case, however, the spectral width of the harmonics is more than 10 eV wide, which deteriorates the lateral resolution of the microscope due to the chromatic aberration of the immersion lens. If we use 20 fs pulses instead, as in the above HHG experiments, the spectral width of the harmonics drops to less than 1 eV, which considerably reduces the effect of chromatic aberration. Nevertheless, we may still have to cope with the issue of space charges in the microscope, which can be counteracted by optimizing the light pulse train with respect to pulse height and repetition frequency. For PEEM imaging an increase in pulse dispersion and repetition rate is certainly more favorable than an increase in pulse height. This opens a pathway to realize element-selective magnetic microscopy with femtosecond time resolution in the laboratory.

1.4 Conclusions

The magnetodynamics in magnetic heterosystems is determined by a complex interplay of competing length and time scales as well as the magnetic coupling mechanism. Element- and layer-selective techniques are mandatory to discriminate the

individual microscopic processes governing the dynamic behavior. Our experiments show that time-resolved soft X-ray photoemission microscopy has matured as a versatile tool to address the various aspects of magnetization dynamics on small length scales and down to the picosecond regime. A further extension of this imaging approach into the subpicosecond regime seems feasible with the use of higher harmonic generation-based light sources. This will give a laterally resolved access to the highly interesting area of ultrafast demagnetization phenomena and optically driven switching processes.

Acknowledgements This review covers extensive research activities which have run for several years involving a large number of collaborators. I am indebted to R. Adam, P. Grychtol, D. Rudolf, S. Cramm, I. Krug, and C. Wiemann, as well as M. Aeschlimann (University of Kaiserlautern), S. Mathias (University of Kaiserlautern), T. Silva (NIST Boulder), J.M. Shaw (NIST Boulder), H.T. Nembach (NIST Boulder), C. La-O-Vorakiat (JILA Boulder), E. Turgut (JILA Boulder), M.M. Murnane (JILA Boulder), H.C. Kapteyn (JILA Boulder) A. Kaiser (ALS Berkeley), A. Krasyuk (MPI Halle), and G. Schönhense (University of Mainz) for their collaboration and scientific discussions.

Thanks are due to B. Küpper, C. Bickmann, J. Lauer, H. Pfeifer, and F.-J. Köhne for expert technical assistance. A particular acknowledgement goes to R. Schreiber for skillful sample growth and preparation.

Financial support by the German Ministry of Education and Research (BMBF) under Grant No. 05KS7UK1 and the German Research Foundation (DFG) through Collaborative Research Centre SFB 491 is gratefully acknowledged.

References

1. R. Wood, J. Magn. Magn. Mater. **321**, 555 (2009)
2. K.Z. Gao, O. Heinonen, Y. Chen, J. Magn. Magn. Mater. **321**, 495 (2009)
3. I.C.T. Results. New logic: the attraction of magnetic computation (2008). <http://www.sciencedaily.com/releases/2008/07/080708094128.htm>
4. S.E. Russek, R.D. McMichael, M.J. Donahue, S. Kaka, in *Spin Dynamics in Confined Magnetic Structures*, vol. II (Springer, Berlin, 2003)
5. D.L. Mills, S.M. Rezende, in *Spin Dynamics in Confined Magnetic Structures*, vol. II (Springer, Berlin, 2003)
6. M.D. Stiles, J. Miltat, in *Spin Dynamics in Confined Magnetic Structures*, vol. III (Springer, Berlin, 2006)
7. G.P. Zhang, W. Hübner, E. Beaurepaire, J.Y. Bigot, in *Spin Dynamics in Confined Magnetic Structures*, vol. I (Springer, Berlin, 2002)
8. E. Beaurepaire, J.C. Merle, A. Daunois, J.Y. Bigot, Phys. Rev. Lett. **76**, 4250 (1996)
9. E. Carpene, E. Mancini, C. Dallera, M. Brenna, E. Puppin, S. De Silvestri, Phys. Rev. B **78**, 174422 (2008)
10. M. Krauss, T. Roth, S. Alebrand, D. Steil, M. Cinchetti, M. Aeschlimann, H.C. Schneider, Phys. Rev. B **80**, 180407 (2009)
11. B. Koopmans, G. Malinowski, F. Dalla Longa, D. Steiauf, M. Fähnle, T. Roth, M. Cinchetti, M. Aeschlimann, Nat. Mater. **9**, 259 (2010)
12. K. Carva, M. Battiatto, P.M. Oppeneer, Phys. Rev. Lett. **107**, 207201 (2011)
13. B.Y. Mueller, T. Roth, M. Cinchetti, M. Aeschlimann, B. Rethfeld, New J. Phys. **13**, 123010 (2011)
14. G.P. Zhang, W. Huebner, G. Lefkidis, Y. Bai, T.F. George, Nat. Phys. **5**, 499 (2009)
15. J.Y. Bigot, M. Vomir, E. Beaurepaire, Nat. Phys. **5**, 515 (2009)

16. M. Battiatto, K. Carva, P.M. Oppeneer, Phys. Rev. Lett. **105**, 027203 (2010)
17. A.V. Kimel, A. Kirilyuk, A. Tsvetkov, R.V. Pisarev, T. Rasing, Nature **429**, 850 (2004)
18. A.V. Kimel, A. Kirilyuk, P.A. Usachev, R.V. Pisarev, A.M. Balbashov, T. Rasing, Nature **435**, 655 (2005)
19. C.D. Stanciu, F. Hansteen, A.V. Kimel, A. Kirilyuk, A. Tsukamoto, A. Itoh, T. Rasing, Phys. Rev. Lett. **99**, 047601 (2007)
20. K. Vahaplar, A.M. Kalashnikova, A.V. Kimel, D. Hinzke, U. Nowak, R. Chantrell, A. Tsukamoto, A. Itoh, A. Kirilyuk, T. Rasing, Phys. Rev. Lett. **103**, 117201 (2009)
21. H. Zabel, S.D. Bader, *Magnetic Heterostructures: Advances and Perspectives in Spinstructures and Spintransport*. Springer Tracts in Modern Physics, vol. 228 (2008)
22. F. Wegelin, D. Valdaitsev, A. Krasyuk, S.A. Nepijko, G. Schönhense, H.J. Elmers, I. Krug, C.M. Schneider, Phys. Rev. B **76**, 134410 (2007)
23. J. Stöhr, S. Anders, IBM J. Res. Dev. **44**, 535 (2000)
24. E. Bauer, J. Phys. Condens. Matter **13**, 11391 (2001)
25. G. Schönhense, H.J. Elmers, S.A. Nepijko, C.M. Schneider, Adv. Imaging Electron Phys. **142**, 159 (2006)
26. H.A. Dürr, C.M. Schneider, in *Handbook of Magnetism and Advanced Magnetic Materials*, ed. by H. Kronmüller, S. Parkin, vol. III (Wiley, Chichester, 2007), p. 1367
27. C. Wiemann, A.M. Kaiser, S. Cramm, C.M. Schneider, Rev. Sci. Instrum. **83**, 063706 (2012)
28. G. Schütz, W. Wagner, W. Wilhelm, P. Kienle, R. Zeller, R. Frahm, G. Materlik, Phys. Rev. Lett. **58**, 737 (1987)
29. C. Chen, F. Sette, Y. Ma, S. Modesti, Phys. Rev. B **42**, 7262 (1990)
30. B. Thole, G. van der Laan, G. Sawatzky, Phys. Rev. Lett. **55**, 2086 (1985)
31. G. van der Laan, B. Thole, G. Sawatzky, J. Goedkoop, J. Fuggle, J. Esteva, R. Karnatak, J. Remeika, H. Dabkowska, Phys. Rev. B **34**, 6529 (1986)
32. E. Arenholz, G. van der Laan, R.V. Chopdekar, Y. Suzuki, Phys. Rev. Lett. **98**, 197201 (2007)
33. M.W. Haverkort, N. Hollmann, I.P. Krug, A. Tanaka, Phys. Rev. B **82**, 094403 (2010)
34. F. Nolting, A. Scholl, J. Stöhr, J. Pompeyrine, H. Siegwart, J.P. Locquet, S. Anders, J. Lüning, E. Fullerton, M. Toney, M.R. Scheinfein, H.A. Padmore, Nature **405**, 767 (2000)
35. I.P. Krug, F.U. Hillebrecht, H. Gomonaj, M.W. Haverkort, A. Tanaka, L.H. Tjeng, C.M. Schneider, Europhys. Lett. **81**, 17005 (2008)
36. I.P. Krug, F.U. Hillebrecht, M.W. Haverkort, A. Tanaka, L.H. Tjeng, H. Gomonay, A. Fraile-Rodriguez, F. Nolting, S. Cramm, C.M. Schneider, Phys. Rev. B **78**, 064427 (2008)
37. C. Schneider, A. Kuksov, A. Krasyuk, A. Oelsner, D. Neeb, S. Nepijko, G. Schönhense, J. Morais, I. Mönch, R. Kaltofen, C.D. Nadaï, N. Brookes, Appl. Phys. Lett. **85**, 2562 (2004)
38. D. Neeb, A. Krasyuk, A. Oelsner, S.A. Nepijko, H.J. Elmers, A. Kuksov, C.M. Schneider, G. Schönhense, J. Phys. Condens. Matter **17**, S1381 (2005)
39. W.K. Hiebert, G.E. Ballentine, L. Lagae, R.W. Hunt, M.R. Freeman, J. Appl. Phys. **92**, 392 (2002)
40. A. Kaiser, C. Wiemann, S. Cramm, C.M. Schneider, J. Phys. Condens. Matter **21**, 314008 (2009)
41. K. Honda, S. Kaya, Sci. Rep. Tohoku Univ. **15**, 721 (1926)
42. C. Scheck, L. Cheng, W.E. Bailey, Appl. Phys. Lett. **88**, 252510 (2006)
43. S.W. Yuan, H.N. Bertram, Phys. Rev. B **44**, 12395 (1991)
44. N.L. Schryer, L.R. Walker, J. Appl. Phys. **45**, 5406 (1974)
45. M.J. Donahue, D.G. Porter, OOMMF user's guide, version 1.0. Tech. rep., National Institute of Standards and Technology, Gaithersburg, MD, 1999
46. P. Grünberg, R. Schreiber, Y. Pang, M. Brodsky, H. Sowers, Phys. Rev. Lett. **57**, 2442 (1986)
47. D.E. Bürgler, P. Grünberg, S. Demokritov, M. Johnson, in *Handbook of Magnetic Materials*, ed. by K. Buschow, vol. 13 (Elsevier Science, Amsterdam, 2001), p. 3
48. C.M. Schneider, A. Kaiser, C. Wiemann, C. Tiegs, S. Cramm, J. Electron Spectrosc. Relat. Phenom. **181**, 159 (2010)
49. A. Kaiser, C. Wiemann, S. Cramm, C.M. Schneider, J. Appl. Phys. **109**, 07D305 (2011)

50. A.M. Kaiser, C. Schöppner, F.M. Römer, C. Hassel, C. Wiemann, S. Cramm, F. Nickel, P. Grychtol, C. Tiege, J. Lindner, C.M. Schneider, Phys. Rev. B **84**, 134406 (2011)
51. W.D. Doyle, E. Stinnett, C. Dawson, L. He, J. Magn. Soc. Jpn. **22**, 91 (1998)
52. T.A. Moore, M.J. Walker, A.S. Middleton, J.A.C. Bland, J. Appl. Phys. **97**, 053903 (2005)
53. J. Vogel, S. Cherifi, S. Pizzini, F. Romanens, J. Camarero, F. Petrucci, S. Heun, A. Locatelli, J. Phys. Condens. Matter **19**, 476204 (2007)
54. F. Dalla Longa, J.T. Kohlhepp, W.J.M. de Jonge, B. Koopmans, Phys. Rev. B **75**, 224431 (2007)
55. G. Lefkidis, G.P. Zhang, W. Huebner, Phys. Rev. Lett. **103**, 217401 (2009)
56. G. Malinowski, F. Dalla Longa, J.H.H. Rietjens, P.V. Paluskar, R. Huijink, H.J.M. Swagten, B. Koopmans, Nat. Phys. **4**, 855 (2008)
57. B. Koopmans, J.J.M. Ruigrok, F.D. Longa, W.J.M. de Jonge, Phys. Rev. Lett. **95**, 267207 (2005)
58. W. Ackermann, G. Asova, V. Ayvazyan, A. Azima, N. Baboi, J. Bähr, V. Balandin, B. Beutner, A. Brandt, A. Bolzmann, R. Brinkmann, O.I. Brovko, M. Castellano, P. Castro, L. Catani, E. Chiadroni, S. Choroba, A. Cianchi, J.T. Costello, D. Cubaynes, J. Dardis, W. Decking, H. Delsim-Hashemi, A. Delserieys, G.D. Pirro, M. Dohlus, S. Düsterer, A. Eckhardt, H.T. Edwards, B. Faatz, J. Feldhaus, K. Flöttmann, J. Frisch, L. Fröhlich, T. Garvey, U. Gensch, C. Gerth, M. Görler, N. Golubeva, H.J. Grabosch, M. Grecki, O. Grimm, K. Hacker, U. Hahn, J.H. Han, K. Honkavaara, T. Hott, M. Hüning, Y. Ivanisenko, E. Jaeschke, W. Jalmuzna, T. Jezynski, R. Kammering, V. Katalev, K. Kavanagh, E.T. Kennedy, S. Khodyachykh, K. Klose, V. Kocharyan, M. Köfer, M. Kollewe, W. Koprek, S. Korepanov, D. Kostin, M. Krassilnikov, G. Kube, M. Kuhlmann, C.L.S. Lewis, L. Lilje, T. Limberg, D. Lipka, F. Löhl, H. Luna, M. Luong, M. Martins, M. Meyer, P. Michelato, V. Miltchev, W.D. Möller, L. Monaco, W.F.O. Müller, O. Napieralski, O. Napoly, P. Nicolosi, D. Nölle, T. Nuñez, A. Oppelt, C. Pagani, R. Paparella, N. Pchalek, J. Pedregosa-Gutierrez, B. Petersen, B. Petrosyan, G. Petrosyan, L. Petrosyan, J. Pfüger, E. Plönjes, L. Poletto, K. Pozniak, E. Prat, D. Proch, P. Pucyk, P. Radcliffe, H. Redlin, K. Rehlich, M. Richter, M. Roehrs, J. Roensch, R. Romaniuk, M. Ross, J. Rosssbach, V. Rybníkov, M. Sachwitz, E.L. Saldin, W. Sandner, H. Schlarb, B. Schmidt, M. Schmitz, P. Schmüser, J.R. Schneider, E.A. Schneidmiller, S. Schnepf, S. Schreiber, M. Seidel, D. Sertore, A.V. Shabunov, C. Simon, S. Simrock, E. Sombrowski, A.A. Sorokin, P. Spanknebel, R. Spesyvtsev, L. Staykov, B. Steffen, F. Stephan, F. Stulle, H. Thom, K. Tiedtke, M. Tischer, S. Toleikis, R. Treusch, D. Trines, I. Tsakov, E. Vogel, T. Weiland, H. Weise, M. Wellhöfer, M. Wendt, I. Will, A. Winter, K. Wittenburg, W. Wurth, P. Yeates, M.V. Yurkov, I. Zagorodnov, K. Zapfe, Nat. Photonics **1**, 336 (2007)
59. H.N. Chapman, A. Barty, M.J. Bogan, S. Boutet, M. Frank, S.P. Hau-Riege, S. Marchesini, B.W. Woods, S. Bajt, W.H. Benner, R.A. London, E. Plonjes, M. Kuhlmann, R. Treusch, S. Dusterer, T. Tschentscher, J.R. Schneider, E. Spiller, T. Moller, C. Bostedt, M. Hoener, D.A. Shapiro, K.O. Hodgson, D. van der Spoel, F. Burmeister, M. Bergh, C. Caleman, G. Huldt, M.M. Seibert, F.R.N.C. Maia, R.W. Lee, A. Szoke, N. Timneanu, J. Hajdu, Nat. Phys. **2**, 839 (2006)
60. A. Locatelli, T.O. Mentes, M.A. Nino, E. Bauer, Ultramicroscopy **111**, 1447 (2011)
61. S. Khan, K. Holldack, T. Kachel, R. Mitzner, T. Quast, Phys. Rev. Lett. **97**, 074801 (2006)
62. C. Stamm, T. Kachel, N. Pontius, R. Mitzner, T. Quast, K. Holldack, S. Khan, C. Lupulescu, E.F. Aziz, M. Wietstruk, H.A. Durr, W. Eberhardt, Nat. Mater. **6**, 740 (2007)
63. C. Boeglin, E. Beaurepaire, V. Halte, V. Lopez-Flores, C. Stamm, N. Pontius, H.A. Durr, J.Y. Bigot, Nature **465**, 458 (2010)
64. T. Pfeifer, C. Spielmann, G. Gerber, Rep. Prog. Phys. **69**, 443 (2006)
65. T. Popmintchev, M.C. Chen, P. Arpin, M.M. Murnane, H.C. Kapteyn, Nat. Photonics **4**, 822 (2010)
66. M. Pretorius, J. Friedrich, A. Ranck, M. Schroeder, J. Voss, V. Wedemeier, D. Spanke, D. Knabben, I. Rozhko, H. Ohldag, F.U. Hillebrecht, E. Kisker, Phys. Rev. B **55**, 14133 (1997)
67. P. Grychtol, R. Adam, S. Valencia, S. Cramm, D.E. Buerger, C.M. Schneider, Phys. Rev. B **82**, 054433 (2010)

68. P. Grychtol, R. Adam, A.M. Kaiser, S. Cramm, D.E. Buerger, C.M. Schneider, J. Electron Spectrosc. Relat. Phenom. **184**, 287 (2011)
69. R. Adam, P. Grychtol, S. Cramm, C.M. Schneider, J. Electron Spectrosc. Relat. Phenom. **184**, 291 (2011)
70. C. La-O-Vorakiat, M. Siemens, M.M. Murnane, H.C. Kapteyn, S. Mathias, M. Aeschlimann, P. Grychtol, R. Adam, C.M. Schneider, J.M. Shaw, H. Nembach, T.J. Silva, Phys. Rev. Lett. **103**, 257402 (2009)
71. S. Mathias, C. La-O-Vorakiat, P. Grychtol, P. Granitzka, E. Turgut, J.M. Shaw, R. Adam, H.T. Nembach, M.E. Siemens, S. Eich, C.M. Schneider, T.J. Silva, M. Aeschlimann, M.M. Murnane, H.C. Kapteyn, Proc. Natl. Acad. Sci. USA **109**, 4792 (2012)
72. S. Mathias, C. La-O-Vorakiat, P. Grychtol, R. Adam, S. Mark, J.M. Shaw, H. Nembach, M. Aeschlimann, C.M. Schneider, T. Silva, M.M. Murnane, H.C. Kapteyn, *OSA Technical Digest* (CD) (Optical Society of America, 2010), p. TuE33
73. B. Koopmans, M. van Kampen, J.T. Kohlhepp, W.J.M. de Jonge, Phys. Rev. Lett. **85**, 844 (2000)
74. C. La-O-Vorakiat, E. Turgut, C.A. Teale, H.C. Kapteyn, M.M. Murnane, S. Mathias, M. Aeschlimann, C.M. Schneider, J.M. Shaw, H.T. Nembach, T.J. Silva, Phys. Rev. X **2**(1), 011005 (2012)
75. F. Hillebrecht, T. Kinoshita, D. Spanke, J. Dresselhaus, C. Roth, H. Rose, E. Kisker, Phys. Rev. Lett. **75**, 2224 (1995)
76. A. Mikkelsen, J. Schwenke, T. Fordell, G. Luo, K. Klunder, E. Hilner, N. Anttu, A.A. Zakharov, E. Lundgren, J. Mauritsson, J.N. Andersen, H.Q. Xu, A. L'Huillier, Rev. Sci. Instrum. **80**, 123703 (2009)



<http://www.springer.com/978-3-642-34957-7>

Nanostructured Materials for Magnetoelectronics

Aktas, B.; Mikailzade, F. (Eds.)

2013, XIV, 220 p., Hardcover

ISBN: 978-3-642-34957-7